Res Chem Intermed (2017) 43:3775–3786
DOI 10.1007/s11164-016-2846-7

Assessment of the intrinsic interactions of mesoporous silica with carbon dioxide

Imene Terrab[1,2] · Rachida Ouargli[1,3] · Bouhadjar Boukoussa[1,3] · Kamel Ghomari[1,2,3] · Rachida Hamacha[1] · René Roy[2] · Abdelkrim Azzouz[2] · Abdelkader Bengueddach[1]

Received: 4 November 2016 / Accepted: 21 December 2016 / Published online: 3 January 2017
© Springer Science+Business Media Dordrecht 2017

Abstract Three mesoporous silica, SBA-16, SBA-15 and MCM-41, with different structures and porosities were synthesized via a hydrothermal method and their interactions with carbon dioxide (CO_2) were investigated through thermal programmed desorption (TPD) and differential scanning calorimetry. TPD measurements provided precise assessments of the intrinsic affinity towards CO_2, without the influence of moisture. All silica materials were found to exhibit intrinsic affinity towards carbon dioxide, but the surface basicity, expressed in terms of retained CO_2 amount, is markedly influenced by increases in pore size and framework structures. SBA-15 displayed the highest CRC values, explained in terms of larger pore size, lower numbers of acidic out-of plane Si–OH and higher numbers of much less acidic in-plane silanols. These findings provide valuable information for a better understanding of the role of the silica structure in the intrinsic basicity, prior to further modifications for improving the affinity towards CO_2 or merely for catalysis purposes involving CO_2 as reagents, intermediates or products.

Keywords Mesoporous silica · SBA-15 · SBA-16 · MCM-41 · Thermal programmed desorption · Carbon dioxide · Reversible capture

✉ Bouhadjar Boukoussa
bbouhdjer@yahoo.fr

[1] Laboratoire de Chimie des Matériaux L.C.M, Université d'Oran1 Ahmed Ben Bella, El-Mnaouer, BP 1524, 31000 Oran, Algeria

[2] Nanoqam, Department of Chemistry, University of Quebec at Montreal, Montréal H3C3P8, Canada

[3] Département de Génie des Matériaux, Faculté de Chimie, Université des Sciences et de la Technologie Mohamed Boudiaf, El-Mnaouer, BP 1505, Oran, Algeria

Introduction

Industrial gas emissions have become a major environmental issue, attracting the interest of scientists throughout the world. Petrochemical industries are an important source of atmospheric pollutants, and carbon dioxide (CO_2) accounts for a large proportion of gas emissions. CO_2 is now recognized as being a major greenhouse gas of anthropogenic origin with large contributions to global warming [1, 2]. This has stimulated scientists to focus interest towards the development of CO_2 capturing methods [3]. Among these, adsorption on porous materials turns out to be a promising and more advantageous route as compared to absorption by base-like liquids such as amines. Because adsorption is strongly dependent on the extent of the contact surface between CO_2 and the solid adsorbents, mesoporous silicas [4–7], zeolites [8–11], MOF [12–14], clays [15–19], carbon materials [20, 21], metal oxides [22–24], solid amines [25, 26] and other materials appear as interesting candidates for this purpose.

To date, different methods have been developed to improve the CO_2 retention capacity (CRC) of adsorbents, some of them involving material functionalization [27, 28], impregnation [29, 30] or cationic exchange [8, 9]. We have already demonstrated that the CRC can be strongly influenced by the nature of the organic compounds grafted or merely deposited on the surface of porous solids [4]. It has also been shown that excessive loading in organic moieties displaying high affinity towards CO_2 may paradoxically affect the adsorptive properties of the materials. This was explained in terms of channel blocking in zeolites and counterparts or decay in the CRC as a result of the formation of organic clusters via H-bridges on clay minerals [15–19].

Here, the choice of the incorporated organic moieties and their concentrations is expected to play a key role in CO_2 capture. However, the solid support structure is of major importance, as well. In this context, different mesoporous silicas without any surface modification were used as CO_2 adsorbents in order to investigate the interaction of CO_2 molecules with the solid surface. Given the wide application fields of such materials, more particularly in catalysis [31–34], adsorption [35–37] and separation processes [38], the expected findings will be very useful in catalytic organic synthesis reactions involving CO_2 as reactant, intermediate or product.

In the present work, a special interest was devoted to mesoporous silicas, such as SBA-15, SBA-16 and MCM-41, due to their uniform pore diameter, regular pore structure and high surface area (>1000 m^2/g). These features are beneficial for improved surface interaction with CO_2 without diffusion hindrance or significant influence of structure defects. For this purpose, the affinity towards CO_2 was assessed in terms of both CRC and retention strength, using thermal programmed desorption of CO_2. The data were correlated with the structure of the mesoporous materials.

Experimental

Syntheses of MCM-41, SBA-15 and SBA-16

The mesoporous materials were prepared by hydrothermal synthesis using cetyltrimethylammonium bromide (CTABr 99%), pluronic P123 and a P123/F127

mixture as templating agents for MCM-41, SBA-15 and SBA-16, respectively. The procedures are well described in our previously published work [33–38]. All the obtained gels were treated at 100 °C in a Teflon-lined autoclave, 72 h for MCM-41, 24 h for SBA-15 and 48 h for SBA-16. The final products were calcined to remove all traces of the template, as follows: at a 1 °C min^{-1} heat rate up to 550 °C, then maintained at 550 °C for 6 h and further cooled to room temperature.

Samples characterization

X-ray powder diffraction (XRD) patterns of the synthesized samples were recorded on a Siemens D5000 instrument (Co-Kα at 1.7890 Å). The specific surface area and porosity were assessed through nitrogen adsorption–desorption isotherms at the nitrogen boiling point, using a Quantachrome Autosorb equipment. For this purpose, the samples were previously degassed at 80 °C for 24 h under a 10^{-4} Torr vacuum. Infrared analysis of the samples was performed on a Nicolet 6700 FTIR/NXR 967 FT Raman instrument. Scanning electronic microscopy (SEM) was achieved using a Hitachi S-4300SE/N-VP-SEM equipment. Transmission electron microscopy (TEM) was carried out by means of a Jeol JEM-2100F instrument, coupled to a field effect cannon that operated at a 200-kV acceleration voltage and an X-ray energy dispersion spectrometer (EDS). Thermal gravimetric analysis (TGA) was performed using a Q500/Discovery MS instrument under a 10.0 mL min^{-1} helium stream and a 5 °C min^{-1} heating rate. The desorption heat of CO_2-saturated materials was estimated through differential scanning calorimetry (DSC), under nitrogen flow (50 mL min^{-1}, 48 kPa) at 10 °C min^{-1} heating rate, using a Mettler-Toledo DSC1 Stare System instrument and standard 40 µL aluminum pans.

CO_2 adsorption–desorption tests

Thermal programmed desorption of carbon dioxide (CO_2-TPD) was achieved between 20 and 80 °C (TPD-CO_2 and TPD-H_2O). CO_2 and water retention capacity (CRC and WRC, respectively) were expressed in terms of the area of the corresponding TPD pattern in this temperature range. The choice of this temperature was justified by the main objective of the present work. The latter consisted of estimating the affinity towards CO_2 around ambient conditions in order to achieve truly reversible capture of CO_2 with low or no thermal regeneration. For this purpose, 26 to 46 mg samples were introduced in a tubular Pyrex glass reactor (2 mm internal diameter) [39]. Pure dry CO_2 was injected into a 15 ml min^{-1} nitrogen stream until saturation at 20 °C. The non-adsorbed CO_2 excess was evacuated until there was no detection at the device outlet. After complete purge of the gas excess, TPD measurements were run starting from 20 °C at a 5 °C min^{-1} heating rate under nitrogen flow rates of 1 and 5 ml min^{-1} inside the tubular oven coupled to a dual Li-840A CO_2/H_2O gas analyzer [15].

Results and discussion

Materials structure and morphology

The XRD patterns of SBA-15 and MCM-41 materials show the characteristic peaks of hexagonal phase structure, while that of SBA-16 suggests rather a cubic symmetry (Fig. 1). As a common feature, all materials displayed a strong peak at $2\theta = 2.55°$, 1.04° and 0.73° corresponding to (100) reflection for MCM-41 and SBA-15 and a (110) line for SBA-16, respectively. MCM-41 also showed two weak signals at $2\theta = 4°–5°$ corresponding to (200) and (210) reflections, whereas (110) and (200) lines were observed for SBA-15 around $2\theta = 1.80°–2.06°$. These data provide evidence of the formation of well-ordered mesoporous materials with high hexagonal regularity [31–38].

The lattice parameters were calculated for both MCM-41 and SBA-15 using equation $a_0 = 2d_{100}/\sqrt{3}$ and for SBA-16 by equation $a_0 = \sqrt{2}(d_{110})$ (Table 1). The results obtained were found to fit with the hexagonal p6 mm space group for MCM-41 and SBA-15 and cubic Im3 m space group for SBA-16.

Nitrogen sorption tests revealed type IV isotherms for all samples. This is a specific feature of mesoporous materials according to the classification of IUPAC. However, SBA-15 and SBA-16 display typical H1 and H2 type hysteresis loops at higher relative pressure (Fig. 2a), thereby confirming a capillary condensation within uniform pores in SBA-15 [35, 36] and ink-bottle pores in SBA-16. The BET surface area was found to increase in the following sequence: MCM-41 > SBA-16 > SBA-15, but the pore volume increased in the following order: MCM-41 > SBA-15 > SBA-16. As shown in Fig. 2b, the porous distribution of the obtained materials is quite uniform, showing higher pore homogeneity for both MCM-41 and SBA-16 unlike SBA-15. The BJH method gave pore diameters of ca. 104 Å for SBA-15, 74 Å for SBA-16 and 35 Å for MCM-41, in agreement with data provided by the literature.

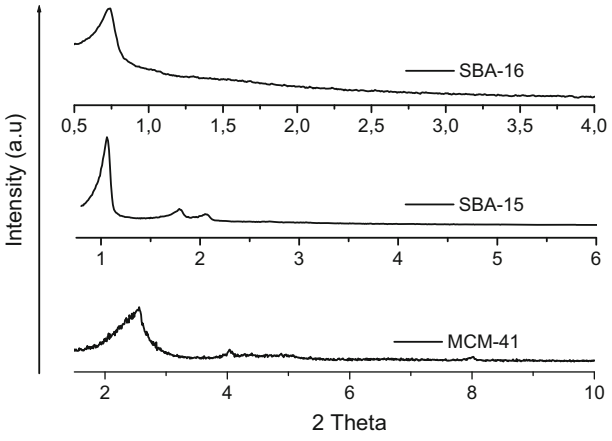

Fig. 1 XRD pattern of MCM-41, SBA-15 and SBA-16

Table 1 Physical characteristics of MCM-41, SBA-15 and SBA-16

Sample	a_0 (Å)[a]	d_{hkl} (Å)	S_{BET} (m^2 g^{-1})[b]	V_{meso} (cc g^{-1})	D_{BJH} (Å)[c]
MCM-41	39.96	34.61	1268	0.9	35
SBA-15	96.11	83.24	577	0.622	104.23
SBA-16	198.58	140.42	980	0.415	74.84

[a] XRD unit cell parameter equals to $a_0 = 2d_{100}/\sqrt{3}$ (for MCM-41 and SBA-15) and to $a_0 = \sqrt{2}(d_{110})$ for SBA-16

[b] BET specific surface

[c] Pore diameter calculated by the BJH method

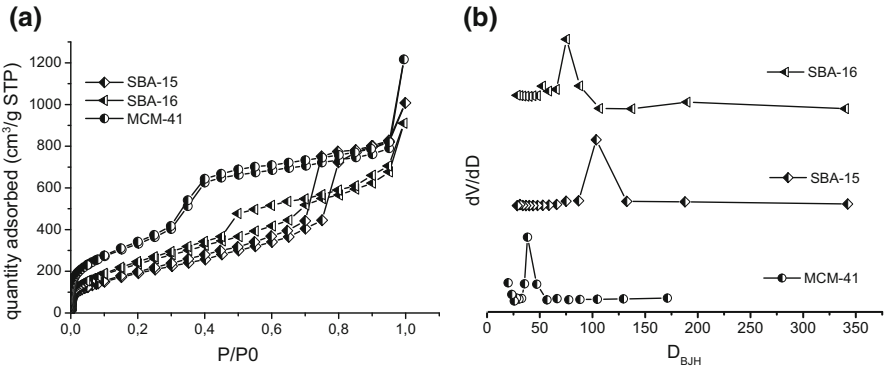

Fig. 2 Nitrogen adsorption–desorption isotherms of MCM-41, SBA-15 and SBA-16

TEM images (Fig. 3) revealed pseudo-spherical particles for MCM-41 (around 50–60 nm) and SBA-16 (and 2–5 μm) and pseudo-hexagonal crystallites for SBA-15 (0.5–0.6 μm). A well-ordered mesoporous structure was observed on TEM images with parallel channels for MCM-41 and SBA-15 and cross-connected channels for SBA-16 (Fig. 4). As expected, TEM images of SBA-16 also revealed a well-ordered cubic mesostructure belonging to the Im3 m symmetry, which is consistent with the result of SEM images. It is worth mentioning the total absence of impurities, thus confirming the reliability of the synthesis procedures used here.

Thermal behavior

TGA measurements gave almost similar thermal profiles for SBA-15 and SBA-16, with slightly higher weight loss of ca. 8–9% for SBA-16 as compared to its counterpart (6–7%). This can be explained by a higher pore volume (0.622 cc g^{-1} vs. 0415) and diameter (104.33 vs. 74.84 Å). The almost total absence of a clear step accounting for the thermal decomposition of pluronic P123 and the P123/F127 mixture indicates the occurrence of polycondensation and pyrolysis processes instead of combustion, due to the use of helium as the carrier gas in the TGA

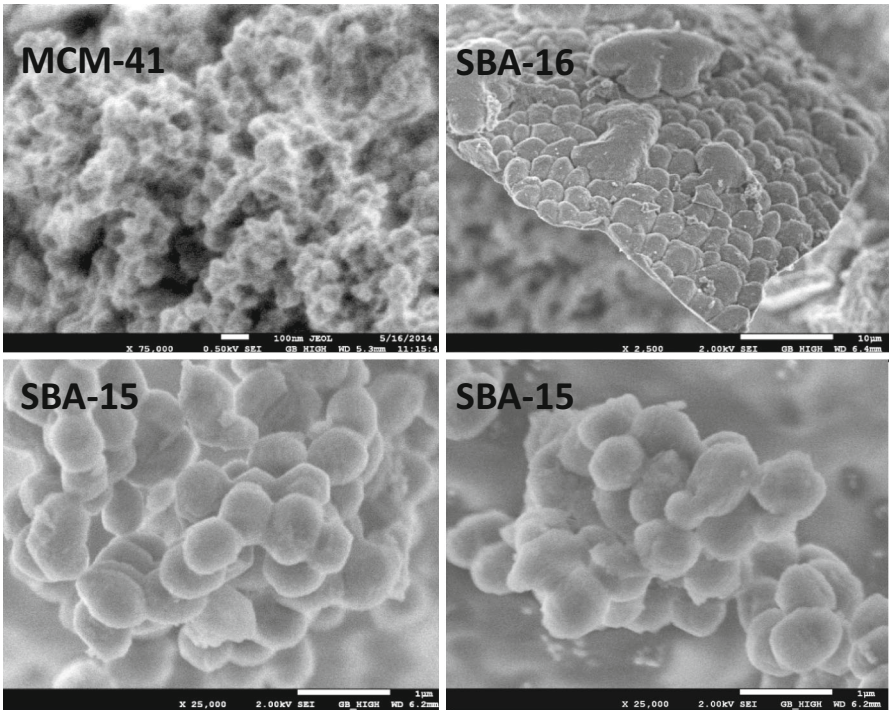

Fig. 3 SEM micrographs of MCM-41, SBA-15, and SBA-16

analysis. This is in agreement with the much higher total weight loss of approximately 58% registered for MCM-41 up to 600 °C (Fig. 5). Here, a possible contribution of the higher specific surface area (1268 $m^2\ g^{-1}$) as compared to SBA-15 (577 $m^2\ g^{-1}$) and SBA-16 (980 $m^2\ g^{-1}$) may be taken into account. Nevertheless, the most plausible explanation resides in additional dehydration due a supposedly higher hydrophilic character of CTABr and partial ammonia release from ammonium group degradation. The higher affinity towards water is supported by the fact that MCM-41 should display a higher number of terminal SiOH, more particularly on the inner surface of the channels [40].

The thermal profile of MCM-41 shows three weight loss steps. Based on previous studies [41], the first step below 140 °C (ca. 3% weight loss) is assigned to the usual dehydration and loss of the adsorbed and included water molecules. The second step observed between 150 and 270 °C must be due to the removal of more retained water due to the supposedly higher hydrophilic character of CTABr-containing MCM-41 as compared to the pure silica counterparts. The third step observed between 350 and 450 °C must account for the continuous decomposition of the template, mainly through ammonia release and pyrolysis, but not from combustion, due to the absence of oxygen.

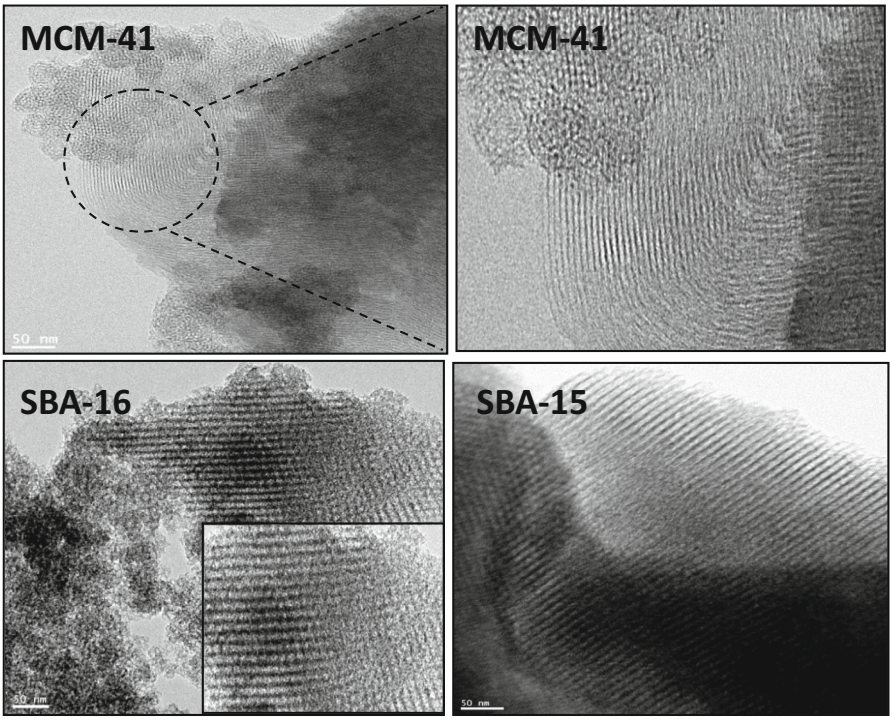

Fig. 4 Transmission electron micrograph of MCM-41, SBA-15, and SBA-16

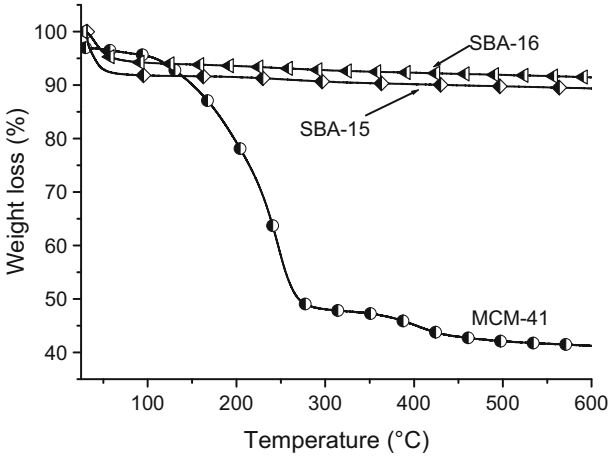

Fig. 5 Thermogravimetric patterns of as-synthesized MCM-41, SBA-15, and SBA-16 solids

Materials interaction with CO_2

CO_2–TPD patterns (Fig. 6a, c, e) show similar shapes for the different mesoporous materials, characterized by the occurrence of a single plateau between ca. 45 and 80 °C, which increased with higher amounts of injected CO_2. An almost two- to three-fold higher plateau was obtained for SBA-15 as compared to MCM-41 and SBA-16. Given the Lewis acid character of CO_2, this suggests a decreasing basicity in the following sequence: SBA-15 > MCM-41 > SBA-16. A possible explanation

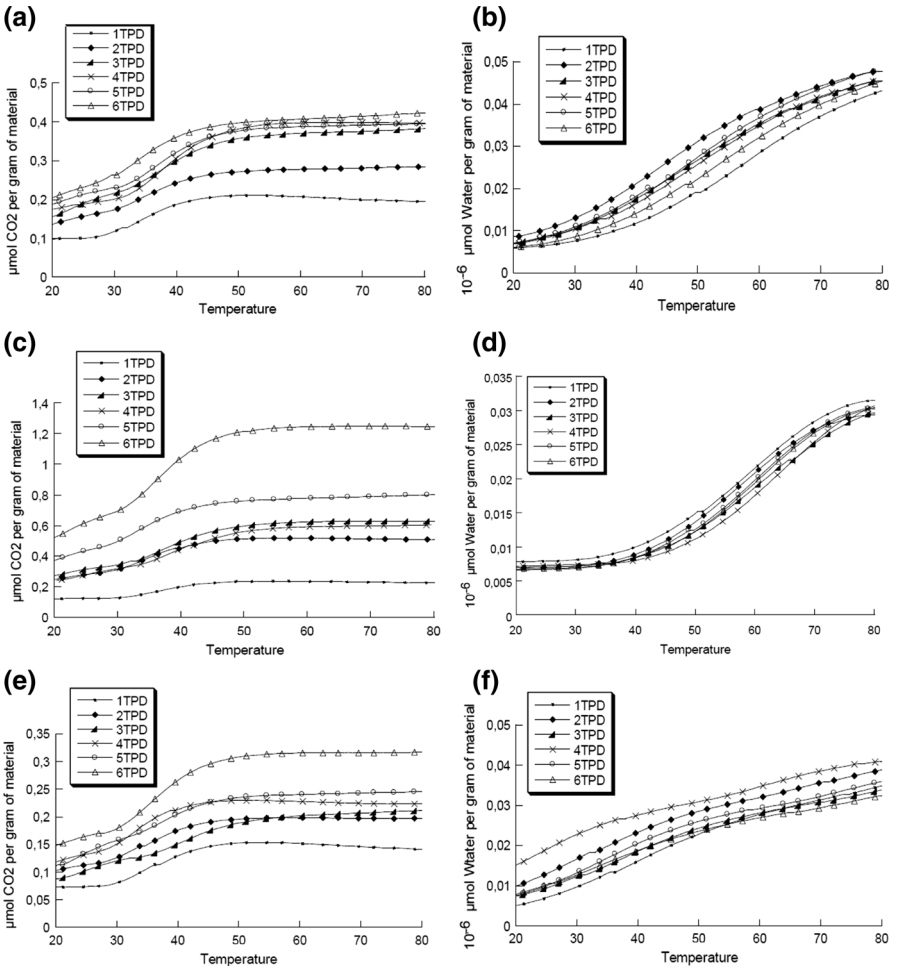

Fig. 6 Temperature programmed desorption of CO_2 and H_2O: **a**, **c**, **e** CO_2–TPD and **b**, **d**, **f** H_2O–TPD of MCM-41, SBA-15 and SBA-16, respectively. These different TPD profiles for both CO_2 and water were achieved at different amounts of dry CO_2 injected (2.4, 85.4, 157.6, 315.3, 472.9 and 788.1 mmol g^{-1}) under similar operating conditions: nitrogen flow rates of 15 mL min^{-1} for injection, 15 mL min^{-1} for purge, 5 mL min^{-1} for TPD. Prior to TPD measurements, dry CO_2 was contacted with 40 mg of fresh SBA-16 samples for 12 h, without any previous dehydration. Both the injection and purge were performed at ambient temperature and pressure.

should consist in higher numbers of out-of-plane Si–OH (pKa 5.6) in MCM-41 and SBA-16. These silanols are known to exhibit higher acidity than their in-plane counterparts (pKa 8.5) [42].

Deconvolution of this plateau revealed a broad desorption peak around 50 °C attributed to weakly basic adsorption sites and another one around 75 °C with slightly stronger basicity, as already reported elsewhere [43]. This appears to be a common feature of all mesoporous silica samples, which must be due to different surface interactions with CO_2 molecules within the investigated temperature range.

It is worth mentioning that, in all cases, CO_2 started desorbing even at ambient temperature, indicating the occurrence of a purely physical interaction. The retained CO_2 can be completely removed upon heating up to 120–130 °C, or without heating and merely through forced convection under a strong nitrogen stream beyond 15 mL min^{-1}, in agreement with previous data [4, 10].

Increasing amounts of dry CO_2 injected did not produce significant changes in the H_2O–TPD patterns (Fig. 6b, d, f). Fluctuations, if any, must be exclusively due to the measurement accuracy of the Li-COR detector within this range of trace amounts (10^{-6} μmol g^{-1}). The lower values of the desorbed amount of water registered (0.005–0.035 c g^{-1}) indicate a slightly lower hydrophilic character of SBA-15 as compared to the two other silica materials. This can be explained at least partly by its lower specific surface area (577 m^2 g^{-1}). At this trace level, one can consider that TPD measurements provided an accurate assessment of only the intrinsic affinity towards carbon dioxide, without the influence of moisture.

Retention capacity

CRC and WRC were found to be dependent on the material structure. As compared to the two other silica materials, SBA-15 displayed higher CRC values ranging from 14.5 to 76 μmol g^{-1} (Table 2). This difference in CRC can be explained partly by the larger pore size of SBA-15 (104 Å), in agreement with the literature [6, 44]. However, this contrasts with its lower specific surface area (577 m^2 g^{-1}), and the most probable explanation should involve the higher numbers of out-of plane Si–OH (pKa 5.6) in MCM-41 and SBA-16, as compared to SBA-15, which must exhibit, in turn, higher numbers of much less acidic in-plane silanols (pKa 8.5) [42].

The lowest basicity of SBA-16 has already been explained by its higher number of acidic out-of-plane silanols [43, 45]. This is supported by DSC measurements, which revealed ca. three-fold stronger CO_2 interaction with SBA-15 (with a desorption heat of 6.491 kcal mol^{-1}) in comparison with those occurring between CO_2 and MCM-41 (2.057 kcal mol^{-1}), and approximately six-fold stronger than those involving CO_2 and SBA-15 (1.113 kcal mol^{-1}) (Table 2). The correlation between TPD and DSC measurements indicates that CO_2 is adsorbed mainly via physical interactions. This result is of great importance, because it provides clear evidence of the role of the silica structure in the intrinsic basicity before proceeding to surface modification by impregnation with dendrimer polyols for improving the affinity towards CO_2 [4, 10].

Table 2 Variation of CRC and WCR with the amount of injected CO_2

Samples	CO_2 injected (ml g^{-1}) 10^3	CRC (μmol g^{-1})	WRC 10^{-6} (μmol g^{-1})	CO_2 desorption heat (kcal mol^{-1})[a]
MCM-41	0.05	13.0	1.5	2.057
	1.66	17.6	2.1	
	3.33	22.7	1.9	
	6.66	23.8	1.9	
	10	24.0	2.1	
	16.66	26.0	2.2	
SBA-15	0.06	14.5	1.2	6.491
	2.25	32.5	1.1	
	4.50	37.8	1.1	
	9.00	38.4	1.1	
	13.51	52.2	1.1	
	22.52	76.0	1.1	
SBA-16	0.03	9.3	1.5	1.113
	1.08	12.6	1.9	
	2.17	13.4	1.8	
	4.34	14.7	2.2	
	6.52	16.5	1.8	
	10.86	19.5	1.6	

[a] CO_2 desorption heat as determined through differential scanning calorimetry of samples saturated overnight with CO_2-saturated at room temperature and pressure

Conclusion

The results obtained here allow concluding that highly pure SBA-15, SBA-16 and MCM-41 silicas exhibit intrinsic affinity towards carbon dioxide. Accurate TPD measurements provided precise assessments of the intrinsic affinity towards carbon dioxide, without the influence of moisture. CO_2 retention appears to be dependent not only on the pore diameter and mesoporosity of solids but also on the silica surface structure. As compared to the two other silica materials, SBA-15 displayed higher CRC values, explained in terms of larger pore size and lower numbers of acidic out-of plane Si–OH, and higher numbers of much less acidic in-plane silanols. TPD and DSC measurements were in agreement, confirming that CO_2 capture involves mainly physical interactions. This result is of great importance, because it provides clear evidence of the intrinsic basicity of silica surfaces prior to further CO_2 affinity improvements.

Acknowledgement This work was supported by a grant from MDEIE-FQRNT to A.A and R.R.

References

1. National Oceanic and Atmospheric Administration. http://www.esrl.noaa.gov/gmd/ccgg/trends/,2013
2. IPCC Fifth Assessment Report: Climate Change 2013, http://www.ipcc.ch/report/ar5/,2013
3. R. Ben-Mansour, M.A. Habib, O.E. Bamidele, M. Basha, N.A.A. Qasem, A. Peedikakkal, T. Laoui, M. Ali, Appl. Energy **161**, 225–255 (2016)
4. K. Ghomari, A. Benhamou, R. Hamacha, A. Bengueddach, S. Nousir, T.C. Shiao, R. Roy, A. Azzouz, Thermochim. Acta **600**, 52–61 (2015)
5. S. Loganathan, M. Tikmani, S. Edubilli, A. Mishra, A.K. Ghoshal, Chem. Eng. J. **256**, 1–8 (2014)
6. S. Loganathan, M. Tikmani, A.K. Ghoshal, Chem. Eng. J. **280**, 9–17 (2015)
7. R. Sanz, G. Calleja, A. Arencibia, E.S. Sanz-Perez, Microporous Mesoporous Mater. **209**, 165–171 (2015)
8. A. Khelifa, Z. Derriche, A. Bengueddach, Microporous Mesoporous Mater. **32**, 199–209 (1999)
9. R. Ghezini, M. Sassi, A. Bengueddach, Microporous Mesoporous Mater. **113**, 370–377 (2008)
10. I. Terrab, B. Boukoussa, R. Hamacha, N. Bouchiba, R. Roy, A. Bengueddach, A. Azzouz, Thermochim. Acta **624**, 95–101 (2016)
11. M. Kacem, M. Pellerano, A. Delebarre, Fuel Process. Technol. **138**, 271–283 (2015)
12. Z. Chen, K. Adil, Ł.J. Weselinski, Y. Belmabkhout, M. Eddaoudi, J. Mater. Chem. A **3**, 6276 (2015)
13. B.A. Al-Maythalony, O. Shekhah, R. Swaidan, Y. Belmabkhout, I. Pinnau, M. Eddaoudi, J. Am. Chem. Soc. **137**, 1754–1757 (2015)
14. L. Fu, G. Qi, O. Shekhah, Y. Belmabkhout, L. Estevez, M. Eddaoudi, E.P. Giannelis, ChemSusChem **7**, 1035–1037 (2014)
15. A. Azzouz, S. Nousir, N. Platon, K. Ghomari, T.C. Shiao, G. Hersant, J.-Y. Bergeron, R. Roy, Int. J. Greenhouse Gas Control **17**, 140–147 (2013)
16. A. Azzouz, N. Platon, S. Nousir, K. Ghomari, D. Nistor, T.C. Shiao, R. Roy, Sep. Purif. Technol. **108**, 181–188 (2013)
17. A. Azzouz, E. Assaad, A.-V. Ursu, T. Sajin, D. Nistor, R. Roy, Appl. Clay Sci. **48**, 133–137 (2010)
18. S. Nousir, N. Platon, K. Ghomari, A.-S. Sergentu, T.C. Shiao, G. Hersant, J.-Y. Bergeron, R. Roy, A. Azzouz, J. Colloids Interface Sci. **402**, 215–222 (2013)
19. A. Azzouz, A.-V. Ursu, D. Nistor, T. Sajin, E. Assaad, R. Roy, Thermochim. Acta **496**, 45–49 (2009)
20. S.-M. Hong, G. Lim, S.H. Kim, J.H. Kim, K.B. Lee, H.C. Ham, Microporous Mesoporous Mater. **219**, 59–65 (2016)
21. N. Díez, P. Álvarez, M. Granda, C. Blanco, R. Santamaría, R. Menéndez, Chem. Eng. J. **281**, 704–712 (2015)
22. A. Hanif, S. Dasgupta, A. Nanoti, Chem. Eng. J. **280**, 703–710 (2015)
23. W.N. Roslam, W. Isahak, Z.A. CheRamli, M.W. Ismail, K. Ismail, R.M. Yusop, M.W. Mohamed Hisham, M.A. Yarmo, J. CO2 Util. **2**, 8–15 (2013)
24. L.K. Gopalakrishna Bhatta, S. Subramanyam, M.D. Chengala, S. Olivera, K. Venkatesh, J. Clean. Prod. **103**, 171–196 (2015)
25. K. Li, J. Jiang, S. Tian, F. Yan, X. Chen, J. Mater. Chem. A. **3**, 2166–2175 (2015)
26. K. Li, J. Jiang, F. Yan, S. Tian, X. Chen, Appl. Energy **136**, 750–755 (2014)
27. N. Gargiulo, A. Verlotta, A. Peluso, P. Aprea, D. Caputo, Microporous Mesoporous Mater. **215**, 1–7 (2015)
28. R. Kishor, A.K. Ghoshal, Chem. Eng. J. **262**, 882–890 (2015)
29. I.H. Arellano, S. HadiMadani, J. Huang, P. Pendleton, Chem. Eng. J. **283**, 692–702 (2016)
30. A. Zukal, J. Pastva, J. Čejka, Microporous Mesoporous Mater. **167**, 44–50 (2013)
31. B. Boukoussa, N. Aouad, R. Hamacha, A. Bengueddach, J. Phys. Chem. Solids **78**, 78–83 (2015)
32. B. Boukoussa, F. Sebih, R. Hamacha, S. Bellahouel, A. Derdour, A. Bengueddach, Res ChemIntermed. **41**, 2221–2233 (2015)
33. B. Boukoussa, S. Zeghada, G. Bentabed Ababsa, R. Hamacha, A. Derdour, A. Bengueddach, F. Mongin, Appl. Catal. A **489**, 131–139 (2015)
34. K. Chikh, B. Boukoussa, L. Bouhadjar, M. Bencheikh, R. Hamacha, R. Meghabar, M. Belbachir, A. Bengueddach, Res ChemIntermed. **41**, 6485–6496 (2015)
35. B. Boukoussa, R. Hamacha, A. Morsli, A. Bengueddach. Arab. J. Chem. http://dx.doi.org/10.1016/j.arabjc.2013.07.049 (2013)
36. N. Bouazizi, R. Ouargli, S. Nousir, R. Ben Slama, A. Azzouz, J. Phys. Chem. Solids **77**, 172–177 (2015)

37. H. Sekkiou, B. Boukoussa, R. Ghezini, Z. Khenchoul, A. Ouali, R. Hamacha, A. Bengueddach, Mater. Res. Expr. **3**, 085501 (2016)
38. R. Ouargli, R. Hamacha, N. Benharrats, A. Boos, A. Bengueddach, J. Porous Mater. **22**, 511–520 (2015)
39. A. Azzouz, D. Nistor, D. Miron, A.V. Ursu, T. Sajin, F. Monette, P. Niquette, R. Hausler, Thermochim. Acta **449**, 27–34 (2006)
40. N.A. Fellenz, J.F. Bengoa, S.G. Marchetti, A. Gervasini, Appl. Catal. A Gen. **435–436**, 187–196 (2012)
41. K.M.S. Khalil, J. Colloids Interface Sci. **315**, 562–568 (2007)
42. M. Sulpizi, M.P. Gaigeot, M. Sprik, J. Chem. Theory Comput. **8**, 1037–1047 (2012)
43. S. Larouk, R. Ouargli, D. Shahidi, L. Olhund, T.C. Shiao, N. Chergui, T. Sehili, R. Roy, A. Azzouz, Catalytic ozonation of Orange-G through highly interactive contributions of hematite and SBA-16—To better understand azo-dye oxidation in nature. Chemosphere, in press, 10.1016/j.chemosphere.2016.11.120 (2016)
44. M. Gu, B. Zhang, Z. Qi, Z. Liu, S. Duan, X. Du, X.F. Xian, Sep. Purif. Technol. **146**, 213–218 (2015)
45. R. Ouargli, S. Larouk, I. Terrab, R. Hamacha, N. Benharrats, A. Bengheddach, A. Azzouz, Ozone Sci. Eng. **38**, 48–61 (2016)